iScience

CellPress
OPEN ACCESS

Article

Porous gold with three-level structural hierarchy

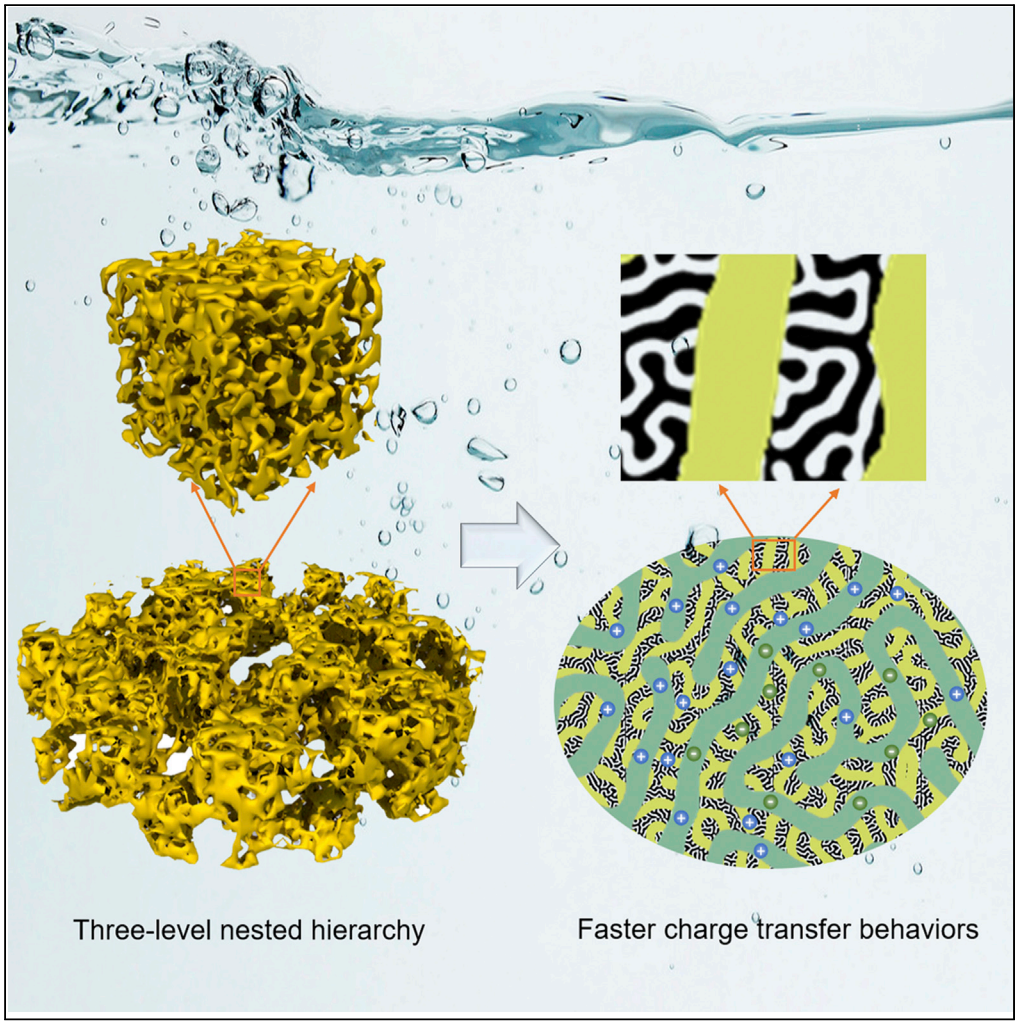

Yujun Shi, Ying Zhang, Bin Yu, Kuibo Yin, Jingyu Qin, Zhonghua Zhang

zh_zhang@sdu.edu.cn

Highlights

N^3PG with three-level structural hierarchy was fabricated based on VPD and ECD

The ligament distribution of N^3PG covers nanometer, submicron and micron scales

The structure superiority of N^3PG is manifested by its faster charge transfer rate

The strategy is of great potential to fabricate other hierarchically porous metals

Shi et al., iScience 25, 105113
October 21, 2022 © 2022 The Author(s).
https://doi.org/10.1016/j.isci.2022.105113

iScience

CellPress
OPEN ACCESS

Article

Porous gold with three-level structural hierarchy

Yujun Shi,[1] Ying Zhang,[1] Bin Yu,[1] Kuibo Yin,[2] Jingyu Qin,[1] and Zhonghua Zhang[1,3,*]

SUMMARY

Facilitating the mass transfer and enlarging the active surface area are two mutually exclusive demands in porous materials, while structural hierarchy could settle this issue by constructing continuous channels with different length scales. However, it is a great challenge to fabricate porous metallic materials with three or more geometrically similar hierarchy levels. Herein, a novel strategy combining vapor phase dealloying with electrochemical dealloying is proposed to achieve nanoporous gold (NPG) with three-level nested hierarchy (N^3PG), in which the length scale covers micron (5866.8 $\pm$ 1445.5 nm), submicron (509.9 $\pm$ 106.0 nm), and nanometer (20.1 $\pm$ 3.0 nm) for each level. Notably, the structural superiority of such material is manifested by its faster charge transfer behaviors, as benchmarked with unimodal and bimodal NPG (N^1PG and N^2PG). The present strategy is of great potential to fabricate other hierarchically porous metals with enhanced functional and structural properties.

INTRODUCTION

Structural hierarchy is popular in nature, such as lotus leaves, conches, snail shells, and so forth, and is also an important structural characteristic of both structural and functional materials (Aziz et al., 2021; Ding and Erlebacher, 2003; Hartmann and Schwieger, 2016; Yilmaz et al., 2015). Special physicochemical properties of materials are associated with their structural hierarchy, such as the super-hydrophobic nature of lotus leaves and structural color of butterfly wings (Song et al., 2018; Yang et al., 2017). In recent years, great advances have been achieved in design, fabrication, and application of hierarchically structured materials (Juarez et al., 2017; Kong et al., 2013; Nyce et al., 2007; Parlett et al., 2013; Qiu et al., 2015; Shi et al., 2017; Sun et al., 2016; Zhang et al., 2019). For example, Zhang et al. (2015) fabricated the hierarchically ordered porous gold membranes consisting of close-packed arrays of nanohole channels (responsible for strong Raman-active sites) and uniformly distributed mesopores (providing efficient binding sites), which exhibit enhanced Raman intensity by a factor of up to 30-fold compared with the commercial Klarite substrate. The hierarchically organized herringbone structure of the eutectic high-entropy alloy could allow reconciliation of crack tolerance and high uniform elongation (An, 2021; Shi et al., 2021a). Moreover, the hierarchical electrodes could minimize the Li dendrite issue and volume change in Li metal batteries (Liu et al., 2019; Xue et al., 2018).

Specially, the regulation and control on the structural hierarchy are of central importance for functional applications of porous materials. Homogeneous non-hierarchical porosity has been demonstrated in nanoporous metals formed by dealloying (Erlebacher et al., 2001; Qian and Chen, 2007), and the smaller pore size promotes the specific surface area and active sites, which however restricts the mass transfer and signal response (Falcucci et al., 2016; Kucernak and Jiang, 2003; Zhang and Li, 2012; Zhang et al., 2011). Combining porosity in different length scales, the structural hierarchy seemingly solves mutually exclusive demands in nanoporous metals (Wada et al., 2018; Wang et al., 2021; Xing et al., 2012; Zhang et al., 2019). Qi et al. (Qi and Weissmüller, 2013) have proved that the nested-network nanoporous gold (NPG) with two different length scales shows a faster charge transport rate than regular NPG. In addition, the structural hierarchy offers new avenue for designing light-weight and high-strength materials. Most recently, Shi et al. (2021b) have unveiled that the stiffness and strength of NPG with two different hierarchy levels are effectively improved compared to the material with a homogeneous structure owing to mitigation in connectivity losing. Furthermore, they have predicted that better mechanical properties could be achieved in NPG with three length scales. However, fabrication of nanoporous metals with three or more geometrically similar hierarchy levels is still a great challenge.

Herein, a novel strategy combining vapor phase dealloying (VPD) with electrochemical dealloying (ECD) is proposed to modulate the structural hierarchy (up to three levels) of porous materials. Taking NPG as an

[1]Key Laboratory for Liquid-Solid Structural Evolution and Processing of Materials (Ministry of Education), School of Materials Science and Engineering, Shandong University, Jingshi Road 17923, Jinan 250061, P.R. China

[2]SEU-FEI Nano-Pico Center, Key Lab of MEMS of Ministry of Education, Southeast University, Nanjing 210096, P.R. China

[3]Lead contact

*Correspondence: zh_zhang@sdu.edu.cn

https://doi.org/10.1016/j.isci.2022.105113

This is an open access article under the CC BY-NC-ND license (http://creativecommons.org/licenses/by-nc-nd/4.0/).

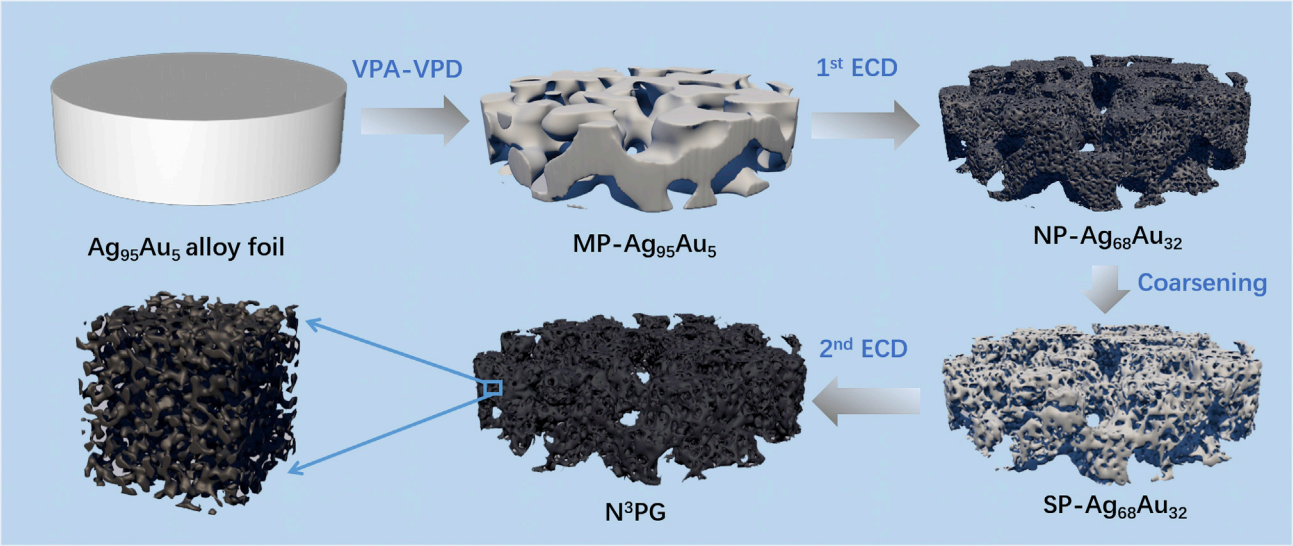

Figure 1. Schematic illustration showing the fabrication strategy of N^3PG

example, besides unimodal (one-level, N^1PG) and bimodal (two-level, N^2PG), a trimodal NPG (three-level, N^3PG) with self-similarity was successfully fabricated, which covers micron, submicron, and nanometer scales of porous structures in one material. The structural hierarchy-related charge transfer behaviors of NPG were further manifested by chronoamperometry measurements, and the charge transfer rate increases with increasing structural hierarchy. Additionally, the solar steam generation (SSG) performance of NPG exhibits no visible dependence with the structural hierarchy increasing.

RESULTS AND DISCUSSION

As illustrated in Figure 1, the proposed strategy combines vapor phase alloying (VPA)-VPD with two-step ECD. Firstly, a dilute solid solution $Ag_{95}Au_5$ alloy was subject to VPA-VPD with Zn as the medium to produce vapor (Shi et al., 2020) and transformed to a microporous structure with unchangeable composition, and the 1st-level hierarchy was well expressed (here, designated as MP-$Ag_{95}Au_5$). During the 1st ECD, Ag was partially dissolved away through control over the applied potential, and a fine nanoporous structure (length scale: ~ 15 nm) was created in the micron-sized ligaments to form a porous Ag-Au alloy (NP-$Ag_{68}Au_{32}$) with the two-level hierarchy. After further annealing, the nanosized ligaments were coarsened to hundreds of nanometers and the obtained alloy was designated as SP-$Ag_{68}Au_{32}$. Subsequently, the SP-$Ag_{68}Au_{32}$ alloy was treated by the 2nd potential-regulated ECD, where most of Ag was removed and the 3rd-level nanopores were produced in the coarsened ligaments. Finally, the N^3PG with the three-level hierarchy was fabricated.

Figures 2A–2D show the macro-morphology variation during the fabrication process of NP-$Ag_{68}Au_{32}$. The pristine $Ag_{95}Au_5$ foil has a smooth and silvery gray surface with metallic luster (Figure 2A), and the X-ray diffraction (XRD) and energy dispersive X-ray (EDX) results show that the alloy precursor has a homogeneous elemental distribution and can be indexed as a face-centered cubic (fcc) Ag (PDF # 65–2871) to form an Ag(Au) solid solution (Figure S1). After VPA with Zn at 550°C for 4 h, an intermetallic compound with a bright silvery surface forms owing to the vapor-induced diffusion and reaction (Figure 2B). Accordingly, the diffraction peak positions and elemental ratio exhibit great similarities with those of the AgZn phase (PDF # 29–1155) in Figures 2E and S2, demonstrating the formation of ($Ag_{95}Au_5$)Zn. A silvery white appearance can be observed on the foil surface after VPD at 650°C for 1 h (Figure 2C). The scanning electron microscopy (SEM) and EDX results (Figures 2F and S3) reveal the formation of micron-scale porosity (several to around 15 microns) running across the whole section of MP-$Ag_{95}Au_5$ without changing the atomic ratio of Ag:Au, indicating the successful fabrication of the 1st-level hierarchy. The above results demonstrate that owing to the equilibrium vapor pressure difference between pure Zn and Ag-Au alloy, Zn in the ($Ag_{95}Au_5$)Zn was selectively evaporated and the remaining Ag and Au atoms diffused and rearranged to form the microporous structure (Lu et al., 2018). Notably, the average ligament size of the 1st

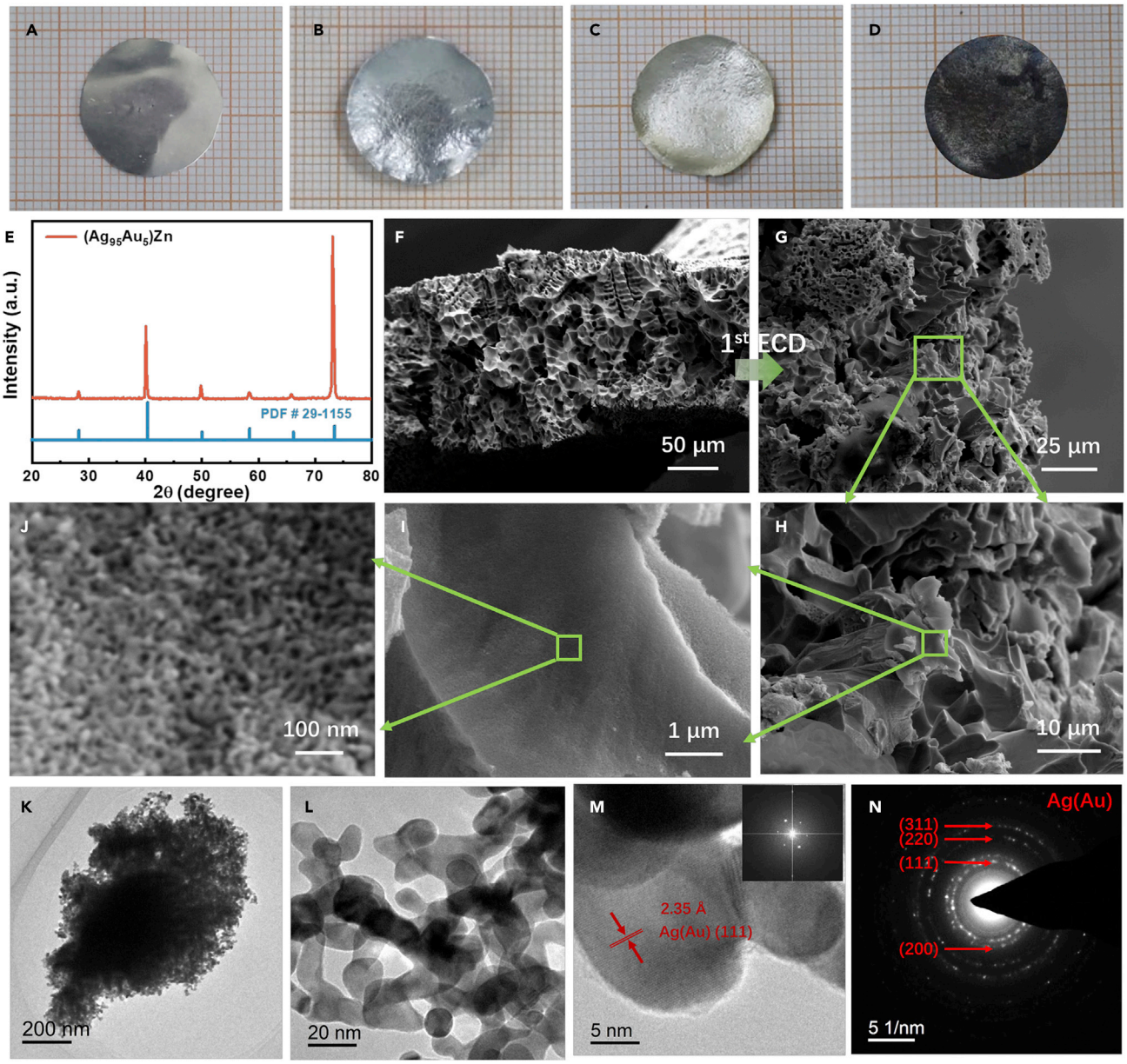

Figure 2. The microstructure characterization of MP-$Ag_{95}Au_5$ and NP-$Ag_{68}Au_{32}$

The optical photographs of (A) pristine $Ag_{95}Au_5$, (B) $(Ag_{95}Au_5)Zn$ after VPA at 550°C for 4 h, (C) MP-$Ag_{95}Au_5$ after VPD of $(Ag_{95}Au_5)Zn$ at 650°C for 1 h, and (D) NP-$Ag_{68}Au_{32}$ after 1st ECD of MP-$Ag_{95}Au_5$ at 0.65 V (vs. Ag/AgCl) in 1 mol L^{-1} $HClO_4$.

(E) XRD pattern of $(Ag_{95}Au_5)Zn$.

(F) SEM image of MP-$Ag_{95}Au_5$.

(G–J) The low- and high-magnification SEM images of NP-$Ag_{68}Au_{32}$.

(K and L) TEM images, (M) HRTEM image, and (N) SAED pattern of NP-$Ag_{68}Au_{32}$. The inset in (M) is the corresponding fast Fourier transform pattern. See also Figures S1–S5.

hierarchy level is smaller than the length scale of pores, which could be associated with the diffusion-limited transport kinetics (Lu et al., 2021). Afterward, a moderate potential of 0.65 V (vs. Ag/AgCl) was applied on the MP-$Ag_{95}Au_5$ alloy to partially dissolve Ag during the 1st ECD in 1 mol L^{-1} $HClO_4$, leading to an absolute black appearance of the as-dealloyed sample (Figure 2D). The stepwise-enlarged SEM images of NP-$Ag_{68}Au_{32}$ in Figures 2G–2J and S4A manifest that a three-dimensional bicontinuous interpenetrating ligament-channel structure is located in the micro-sized 1st-level ligaments with the Ag content of 68.2 at.%

(Figure S4B) well above the parting limit (55.0 at.% Ag) in Ag-Au for dealloying (Artymowicz et al., 2009; Sieradzki et al., 2002). Different from VPD, the 1st ECD was driven by the standard electrode potential difference between Ag and Au, during which partial Ag atoms were dissolved from MP-$Ag_{95}Au_5$ under a moderate potential and the remaining Au and Ag atoms at the low-coordination sites diffused and aggregated to form the nanoporous structure (Qi et al., 2015; Qi and Weissmüller, 2013). The scenario of bimodal NP-$Ag_{68}Au_{32}$ lays the foundation for the 2nd ECD to induce the formation of the 3rd-level porous structure.

Transmission electron microscopy (TEM) was performed to further characterize the microstructure of NP-$Ag_{68}Au_{32}$ (Figures 2K–2N and S4C–S4E). The dark skeletons and bright voids in Figures 2K, 2L, and S4C reveal the formation of the typical interconnected ligament-channel structure. The lattice fringes in the high-resolution TEM (HRTEM) image (Figure 2M and inset) are in good agreement with the (111) crystal plane of Ag(Au) solid solution. The SEM and TEM results jointly demonstrate the formation of the two-level porous hierarchy in NP-$Ag_{68}Au_{32}$. The average ligament size is 15.0 $\pm$ 2.0 nm (Figure S4F) in the 2nd-level hierarchy of NP-$Ag_{68}Au_{32}$. Specially, the selected-area electron diffraction (SAED) pattern in Figure 2N shows obvious diffraction rings that correspond well with the (111), (200), (220), and (311) reflections of Ag(Au), confirming the nanocrystalline nature of NP-$Ag_{68}Au_{32}$. Additionally, through adjusting the time of VPA (550°C for 9 h) to form ($Ag_{95}Au_5$)Zn_3 (Figures S5A and S5B), the bimodal NP-$Ag_{71}Au_{29}$ alloy with a different porous microstructure after VPD-1st ECD can be obtained (Figures S5C–S5F), demonstrating the microstructure adjustability of the 1st-level porosity. The above results illustrate that VPD and ECD cooperate well in fabricating the bimodal structure with the two-level hierarchy (micro- and nanosized pores).

Further processing composed of annealing and 2nd ECD was conducted to obtain N^3PG with three distinct length scales. After annealing at 500°C for 2 h, the nanosized ligaments coarsened to submicron scale (511.9 $\pm$ 88.7 nm) throughout the whole section of SP-$Ag_{68}Au_{32}$ with the silvery appearance and bimodal structure lacking of porosity in nanoscale (Figures 3A, 3B, and S6). The coarsening process is driven by the reduction of the interfacial energy in the form of constant diffusion of Ag and Au atoms (Chen-Wiegart et al., 2012). Subsequently, the 2nd ECD at 1 V (vs. Ag/AgCl) was employed in 1 mol L^{-1} $HClO_4$ to remove most of Ag in SP-$Ag_{68}Au_{32}$. As expected, the 3rd-level nanoporous structure was further created in the submicron ligaments, and the level-by-level SEM images in Figures 3C–3E distinctly show nested porosities of three well-defined length scales in N^3PG. The porosity with the nanoscale runs across the whole ligaments of the 2nd-level hierarchy (Figures 3E, 3F, S7A, and S7B) with only 2.0 at.% Ag residual (Figure S7C) and is dominated by the similar formation mechanism (selective dissolution of Ag and diffusion of Au) with the 2nd-level porosity during the ECD process. TEM characterization further manifests the hierarchically porous structure (2nd-level and 3rd-level) of N^3PG (Figures 3G–3J and S8). The interconnected ligament-channel structure in the 3rd-level can be well identified from the fracture surface and smooth margin of the upper-level ligaments (highlighted by ellipses in Figures 3G and 3H), indicating the successful fabrication of N^3PG. Additionally, the average ligament sizes of three different hierarchy levels are determined as 5866.8 $\pm$ 1445.5, 509.9 $\pm$ 106.0, and 20.1 $\pm$ 3.0 nm, respectively, one order of magnitude larger than their neighboring lower hierarchy levels. The lattice fringes in the HRTEM image and the diffraction rings in the SAED pattern (Figures S8B and S8C) well confirm the formation of the fcc Au in N^3PG. Noticeably, the formation of nanosized ligaments/crystals is related to the broadening of diffraction peaks belonging to NP-$Ag_{68}Au_{32}$ and N^3PG in the XRD patterns (Figure S9).

For comparison, we also fabricated N^1PG and N^2PG by respectively dissolving most of Ag in $Ag_{95}Au_5$ and MP-$Ag_{95}Au_5$ via ECD at 1 V (vs. Ag/AgCl) in 1 mol L^{-1} $HClO_4$. As shown in Figures 4A, 4B, and S10A, the as-obtained N^1PG exhibits a compact section at low magnifications (Figures 4A and S10A), but shows a typical bicontinuous ligament-channel structure at a higher magnification (Figure 4B) and only possesses one-level nanoporosity with a ligament size of 15.4 $\pm$ 2.0 nm. N^2PG shows similar morphologies with NP-$Ag_{68}Au_{32}$ because of the up-front VPA-VPD. Two-level hierarchy networks run through the whole section, including the micron-scale (4870.8 $\pm$ 909.3 nm) and nanometer-scale (23.3 $\pm$ 3.5 nm) ligaments (Figures 4C, 4D, and S10B). The EDX results (Figures S10C and S10D) demonstrate that most Ag atoms were dissolved away and the residual Ag is less than 10 at.% in N^1PG and N^2PG. The TEM images in Figures 4E and 4F further reveal the typical bicontinuous ligament-channel structure of the 2nd-level hierarchy in N^2PG. The HRTEM image (Figure 4G) distinctly shows lattice fringes with a spacing of 2.35 Å, corresponding to the (111) plane of fcc Au. The nanocrystalline nature of the selected area in N^2PG is verified by the corresponding SAED pattern (Figure 4H). Figure 4I compares the ligament size distributions of N^1PG, N^2PG, and N^3PG. Apparently, the

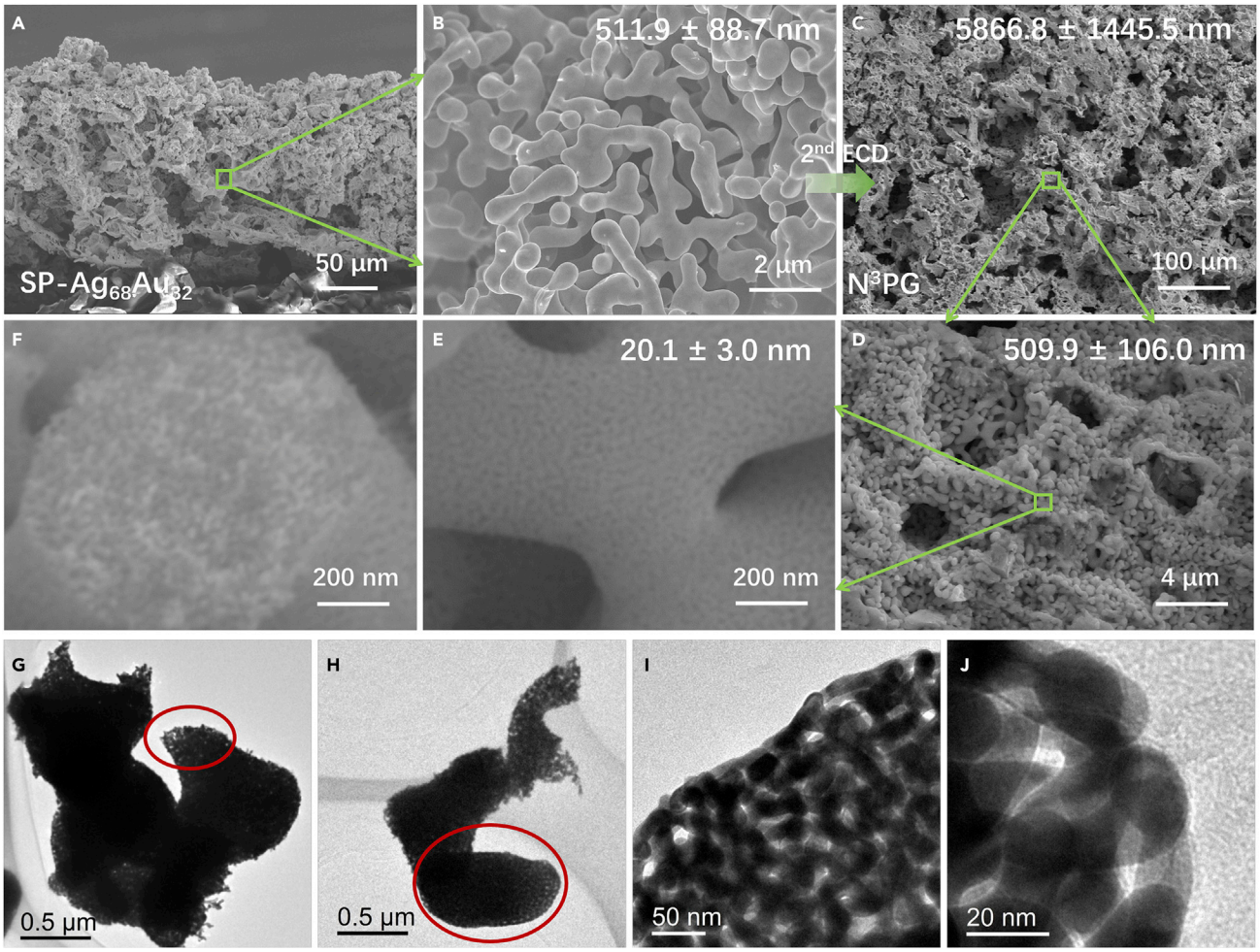

Figure 3. The microstructure characterization of SP-$Ag_{68}Au_{32}$ and N^3PG

(A and B) The low- and high-magnification SEM images of SP-$Ag_{68}Au_{32}$ after annealing at 500°C for 2 h.

(C–F) SEM images showing three different hierarchy levels of N^3PG after the 2nd ECD at 1 V (vs. Ag/AgCl) in 1 mol L^{-1} $HClO_4$.

(G–J) The low- and high-magnification TEM images of N^3PG. See also Figures S6–S9.

N^3PG exhibits a wide-ranged and multi-level distribution of ligaments that are located in nanometer, submicron, and micron scales, respectively, much superior to the monotonic distribution of N^1PG (only the nanometer scale) and the bimodal distribution of N^2PG (nanometer and micron scales). The above results vigorously demonstrate that combining VPD with ECD could effectively regulate the hierarchy levels of porous metallic materials.

To undertake a comprehensive evaluation on the influence of structural hierarchy levels on the mass-transfer and electrochemical active surface area (ECSA), step potential measurements and cyclic voltammetry (CV) scans were performed on N^1PG, N^2PG, and N^3PG in 1 mol L^{-1} $HClO_4$. As shown in Figures 5A–5C (step potentials: 0.1, 0.3, 0.5, 0.8, and 1.0 V (vs. Ag/AgCl)), the currents of N^3PG under each potential decay fastest as benchmarked with N^1PG and N^2PG after potential steps. Specially, it takes about 0.07 s for the N^3PG to decay to half of its initial value at the potential 0.5 V (vs. Ag/AgCl), which is around 1/4 and 1/10 of that for N^2PG (0.27 s) and N^1PG (0.67 s) to reach the same level (Figure 5D). In addition, the total transferred charge of N^2PG and N^3PG is much larger than that of N^1PG at each potential, and the charge difference increases with increasing applied potential (Figure 5E). Moreover, the N^3PG could transfer more charges than N^2PG at higher potentials of 0.8 and 1.0 V (vs. Ag/AgCl), despite their similar transferred charges at lower potentials. The double-layer capacitance (C_{dl}) was measured to assess the ECSA of N^1PG, N^2PG, and N^3PG based on the CV curves in the non-Faradaic region (Figure S11). Figure 5F reveals that the C_{dl}

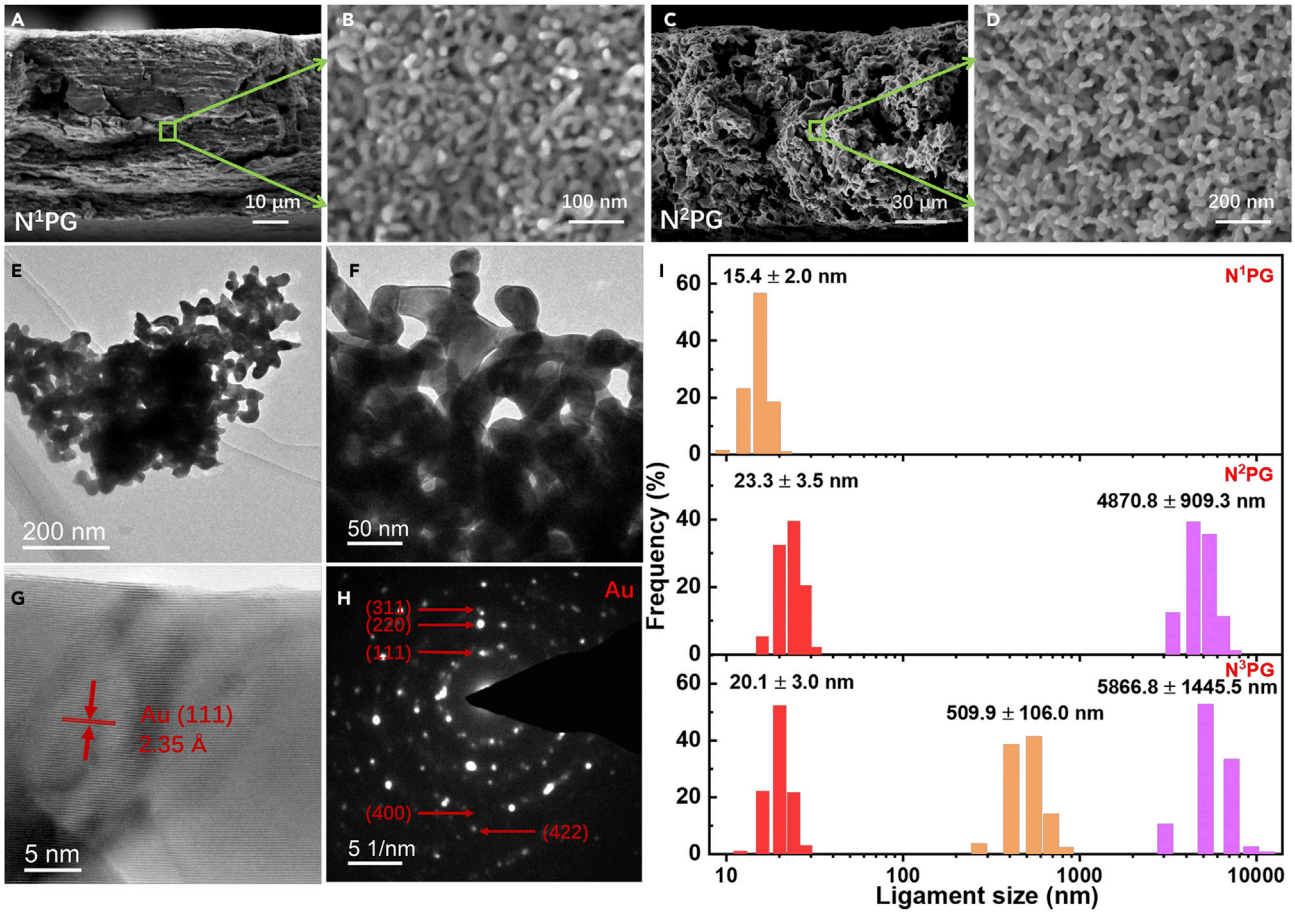

Figure 4. The structural hierarchy level comparison of N^1PG, N^2PG, and N^3PG

(A and B) The low- and high-magnification SEM images of N^1PG after ECD of pristine $Ag_{95}Au_5$ at 1 V (vs. Ag/AgCl) in 1 mol L^{-1} $HClO_4$.

(C and D) The low- and high-magnification SEM images of N^2PG after ECD of MP-$Ag_{95}Au_5$ at 1 V (vs. Ag/AgCl) in 1 mol L^{-1} $HClO_4$.

(E and F) TEM images, (G) HRTEM image, and (H) SAED pattern of N^2PG.

(I) The ligament size distributions of N^1PG, N^2PG, and N^3PG. See also Figure S10.

of N^3PG is 108.2 mF cm^{-2}, a little smaller but still comparable to N^1PG (140.5 mF cm^{-2}) and N^2PG (121.2 mF cm^{-2}) because the micron-scale and submicron-scale pores contribute less to the ECSA than nanopores. Figure 5G schematically summarizes the charge transfer behaviors in the three NPG samples. Because of the unimodal nanoporosity, the movement of charges is severely blocked in N^1PG. In contrast, for the NPG with hierarchically porous structure (especially N^3PG), the interpenetrating pores with the micron- and submicron-scale jointly provide multi-level channels for faster charge transfer, while the nanoscale pores can guarantee the ECSA, demonstrating the functional superiority of N^3PG.

Eventually, we preliminarily evaluated the functional properties of the NPG foils taking the SSG performance as an example, Figures 6, S12, and S13. Figure 6A shows that the mass changes of the three NPG samples increase linearly with time prolonging at the constant light intensity of 1 kW m^{-2}, and no obvious difference can be observed. The water evaporation rate was calculated based on the mass changes over time (Figure 6B). Apparently, the evaporation rate increases rapidly at the beginning and keeps at a stable level within 10 min (average rate: 1.43, 1.50, and 1.51 kg m^{-2} h^{-1} for N^1PG, N^2PG, and N^3PG, respectively). Additionally, the photothermal conversion efficiency (η) can be calculated as the following equation (Ghasemi et al., 2014),

$$\eta = \dot{m} h_{LV} / I$$

where $\dot{m}$ is the evaporation rate, h_{LV} is the total enthalpy of sensible heat and liquid-vapor phase change (2.26 kJ g^{-1}), and I is the average power intensity of incident light. As shown in Figure 6C, the conversion

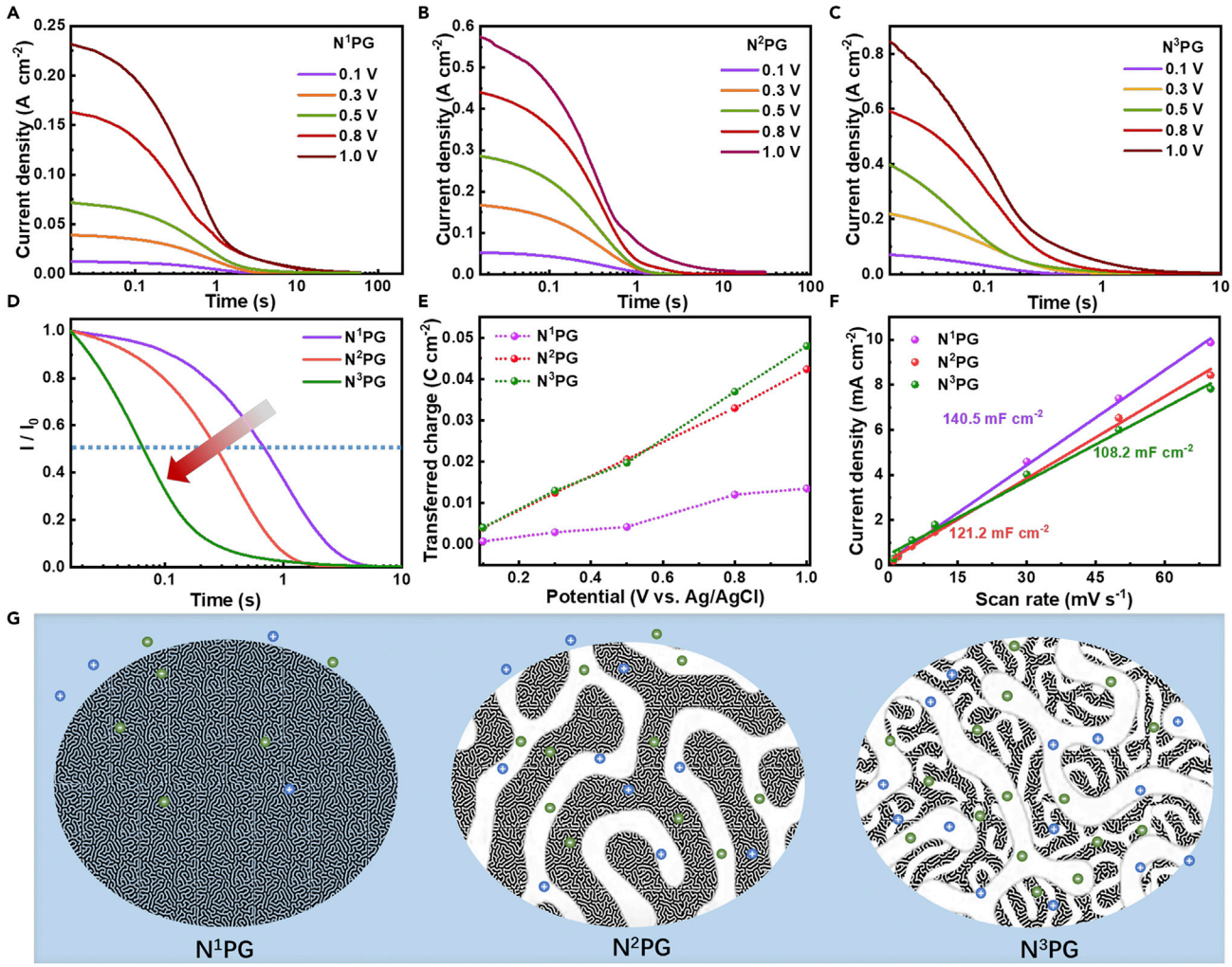

Figure 5. The charge transfer behaviors of N^1PG, N^2PG, and N^3PG

(A–C) The current density-time curves of (A) N^1PG, (B) N^2PG, and (C) N^3PG at different step potentials (0.1, 0.3, 0.5, 0.8, and 1.0 V (vs. Ag/AgCl)).

(D) The current transients of three materials after potential jumping from 0 to 0.5 V (vs. Ag/AgCl).

(E) The transferred charges at different potentials in 0.1 s of N^1PG, N^2PG, and N^3PG.

(F) C_{dl} estimated from the plots of the current density vs. scan rate at 0.35 V (vs. Ag/AgCl).

(G) Schematic diagram showing the charge transfer in N^1PG, N^2PG, and N^3PG. See also Figure S11.

efficiencies of three NPG foils are comparable (94.8%, 94.0%, and 90.2% for N^3PG, N^2PG, and N^1PG, respectively). The infrared images in Figures 6D, S12, and S13 vividly show the quick photothermal response and temperature evolution of N^1PG, N^2PG, and N^3PG. Generally, strong light absorption/conversion ability, sufficient water transport paths, and minimal heat loss are three main factors influencing the SSG performance (Zhang et al., 2022). In our work, the slightly better performance of N^3PG and N^2PG than N^1PG could be attributed to the scenario that the hierarchically porous structure can provide sufficient water transfer paths and efficient broadband light absorption (Wang et al., 2014; Zhu et al., 2019). The present results suggest potential applications of hierarchically porous materials including NPG in SSG.

Conclusion

In summary, the combination of different processes (VPA, VPD, annealing, ECD, etc.) could well regulate the structural hierarchy of porous metals. The NPG with three-level hierarchy and self-similar ligament-channel structure was successfully fabricated for the first time. The length scale of nested ligaments in N^3PG covers the micron, submicron, and nanometer scale, and differs in one order of magnitude with the adjacent. It is worth emphasizing that further optimization of pore sizes at different hierarchy levels

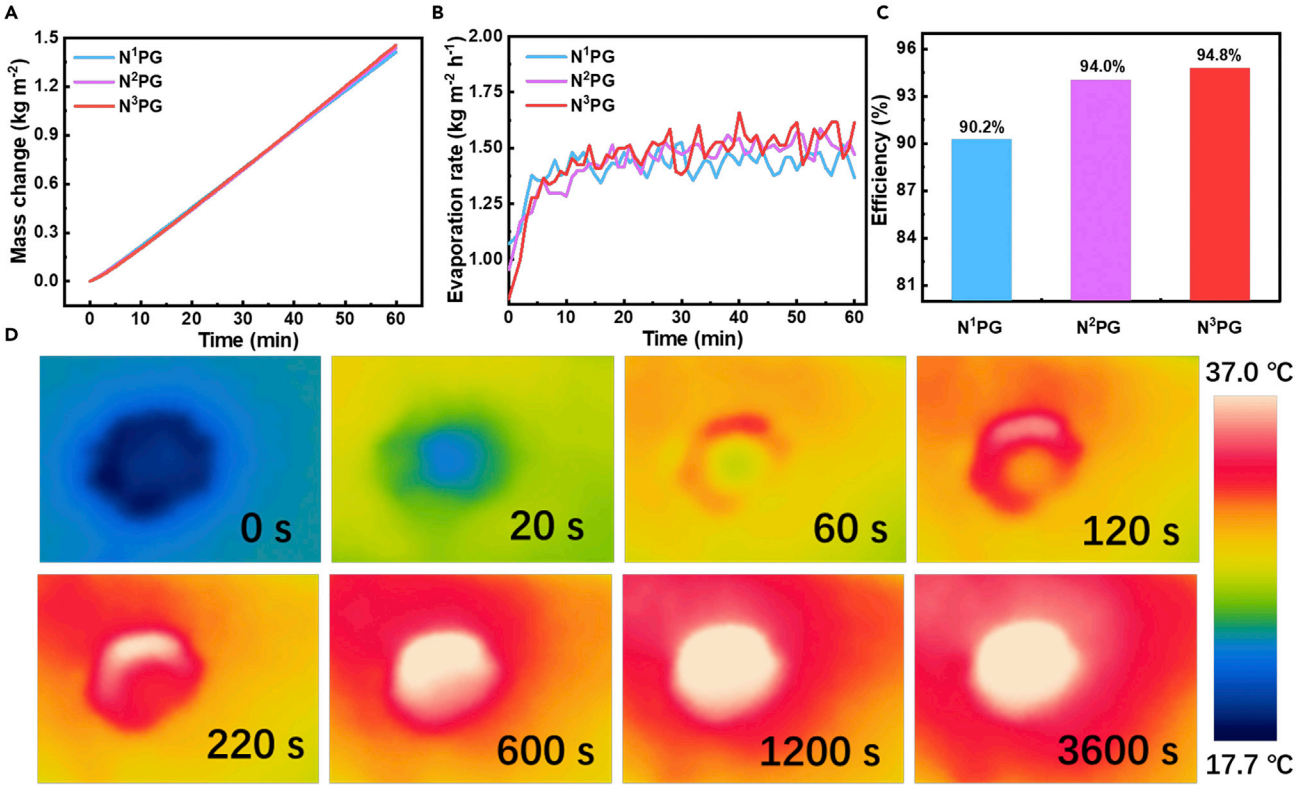

Figure 6. The SSG results of N^1PG, N^2PG, and N^3PG

(A–C) Comparison of (A) mass change, (B) evaporation rate, and (C) photothermal conversion efficiency of N^1PG, N^2PG, and N^3PG under the light intensity of 1 kW m^{-2}.

(D) Infrared images of N^3PG under the light intensity of 1 kW m^{-2}. See also Figures S12 and S13.

is feasible by modulating the process parameters such as the VPA time, dealloying potential, and temperature. The structural superiority of N^3PG has been manifested by its faster charge transfer behaviors as benchmarked with N^1PG and N^2PG. Viewed from improving the functionality and practicability of NPG, three different hierarchy levels could not only better meet the demands of high specific surface area and multi-level channels for mass transfer but also offer opportunities to achieve light-weight and high-strength materials. In addition, the present strategy shows flexibility and universality to prepare other porous metals with multi-level hierarchy.

Limitations of the study

Our strategy successfully fabricated nanoporous gold with three different hierarchy levels. The control over the morphology, size, and homogeneity of the 1st-level hierarchy should be improved. In the follow-up research, an important step could be to further improve the controllability of the structure morphology and investigate the mechanical properties of this material.

STAR★METHODS

Detailed methods are provided in the online version of this paper and include the following:

- KEY RESOURCES TABLE
- RESOURCE AVAILABILITY
  - Lead contact
  - Materials availability
  - Data and code availability
- EXPERIMENTAL MODEL AND SUBJECT DETAILS
- METHOD DETAILS
  - Sample preparation

SUPPLEMENTAL INFORMATION

Supplemental information can be found online at https://doi.org/10.1016/j.isci.2022.105113.

ACKNOWLEDGMENTS

The authors gratefully acknowledge financial support by National Natural Science Foundation of China (51871133), Taishan Scholar Foundation of Shandong Province, the Key Research and Development Program of Shandong Province (2021ZLGX01), and the program of Jinan Science and Technology Bureau (2019GXRC001).

AUTHOR CONTRIBUTIONS

Y.S. prepared the samples, performed the measurements, analyzed the data, and wrote the manuscript. Y.Z. and B.Y. helped with the SSG tests. K.Y. performed the TEM characterization. J.Q. helped to analyze the data. Z.Z. conceived the idea, designed the experiments, and supervised the project. All of the authors have read the manuscript and agreed with its content.

DECLARATION OF INTERESTS

The authors declare no competing interests.

Received: June 16, 2022
Revised: August 29, 2022
Accepted: September 8, 2022
Published: October 21, 2022

REFERENCES

An, X. (2021). Structural hierarchy defeats alloy cracking. Science *373*, 857–858. https://doi.org/10.1126/science.abk1671.

Artymowicz, D.M., Erlebacher, J., and Newman, R.C. (2009). Relationship between the parting limit for dealloying and a particular geometric high-density site percolation threshold. Phil. Mag. *89*, 1663–1693. https://doi.org/10.1080/14786430903025708.

Aziz, A., Carrasco, J., and Grosu, Y. (2021). Towards tuning the modality of hierarchical macro-nanoporous metals by controlling the dealloying kinetics of close-to-eutectic alloys. Phys. Chem. Chem. Phys. *23*, 25388–25400. https://doi.org/10.1039/D1CP03878H.

Chen-Wiegart, Y.-c.K., Wang, S., Chu, Y.S., Liu, W., McNulty, I., Voorhees, P.W., and Dunand, D.C. (2012). Structural evolution of nanoporous gold during thermal coarsening. Acta Mater. *60*, 4972–4981. https://doi.org/10.1016/j.actamat.2012.05.012.

Ding, Y., and Erlebacher, J. (2003). Nanoporous metals with controlled multimodal pore size distribution. J. Am. Chem. Soc. *125*, 7772–7773. https://doi.org/10.1021/ja035318g.

Erlebacher, J., Aziz, M.J., Karma, A., Dimitrov, N., and Sieradzki, K. (2001). Evolution of nanoporosity in dealloying. Nature *410*, 450–453. https://doi.org/10.1038/35068529.

Falcucci, G., Succi, S., Montessori, A., Melchionna, S., Prestininzi, P., Barroo, C., Bell, D.C., Biener, M.M., Biener, J., Zugic, B., and Kaxiras, E. (2016). Mapping reactive flow patterns in monolithic nanoporous catalysts. Microfluid. Nanofluid. *20*, 105. https://doi.org/10.1007/s10404-016-1767-5.

Ghasemi, H., Ni, G., Marconnet, A.M., Loomis, J., Yerci, S., Miljkovic, N., and Chen, G. (2014). Solar steam generation by heat localization. Nat. Commun. *5*, 4449. https://doi.org/10.1038/ncomms5449.

Hartmann, M., and Schwieger, W. (2016). Hierarchically-structured porous materials: from basic understanding to applications. Chem. Soc. Rev. *45*, 3311–3312. https://doi.org/10.1039/c6cs90043g.

Juarez, T., Biener, J., Weissmüller, J., and Hodge, A.M. (2017). Nanoporous metals with structural hierarchy: a review. Adv. Eng. Mater. *19*, 1700389. https://doi.org/10.1002/adem.201700389.

Kong, Q., Lian, L., Liu, Y., and Zhang, J. (2013). Hierarchical porous copper materials: fabrication and characterisation. Micro & Nano Lett. *8*, 432–435. https://doi.org/10.1049/mnl.2013.0113.

Kucernak, A., and Jiang, J. (2003). Mesoporous platinum as a catalyst for oxygen electroreduction and methanol electrooxidation. Chem. Eng. J. *93*, 81–90. https://doi.org/10.1016/s1385-8947(02)00111-0.

Liu, H., Wang, E., Zhang, Q., Ren, Y., Guo, X., Wang, L., Li, G., and Yu, H. (2019). Unique 3D nanoporous/macroporous structure Cu current collector for dendrite-free lithium deposition. Energy Storage Mater. *17*, 253–259. https://doi.org/10.1016/j.ensm.2018.07.010.

Lu, Z., Li, C., Han, J., Zhang, F., Liu, P., Wang, H., Wang, Z., Cheng, C., Chen, L., Hirata, A., et al. (2018). Three-dimensional bicontinuous nanoporous materials by vapor phase dealloying. Nat. Commun. *9*, 276. https://doi.org/10.1038/s41467-017-02167-y.

Lu, Z., Zhang, F., Wei, D., Han, J., Xia, Y., Jiang, J., Zhong, M., Hirata, A., Watanabe, K., Karma, A., et al. (2021). Vapor phase dealloying kinetics of MnZn alloys. Acta Mater. *212*, 116916. https://doi.org/10.1016/j.actamat.2021.116916.

Nyce, G.W., Hayes, J.R., Hamza, A.V., and Satcher, J.H. (2007). Synthesis and characterization of hierarchical porous gold materials. Chem. Mater. *19*, 344–346. https://doi.org/10.1021/cm062569q.

Parlett, C.M.A., Wilson, K., and Lee, A.F. (2013). Hierarchical porous materials: catalytic applications. Chem. Soc. Rev. *42*, 3876–3893. https://doi.org/10.1039/c2cs35378d.

Qi, Z., Vainio, U., Kornowski, A., Ritter, M., Weller, H., Jin, H., and Weissmüller, J. (2015). Porous gold with a nested-network architecture and ultrafine structure. Adv. Funct. Mater. *25*, 2530–2536. https://doi.org/10.1002/adfm.201404544.

Qi, Z., and Weissmüller, J. (2013). Hierarchical nested-network nanostructure by dealloying. ACS Nano *7*, 5948–5954. https://doi.org/10.1021/nn4021345.

Qian, L.H., and Chen, M.W. (2007). Ultrafine nanoporous gold by low-temperature dealloying and kinetics of nanopore formation. Appl. Phys. Lett. *91*, 083105. https://doi.org/10.1063/1.2773757.

Qiu, H.-J., Wang, J.Q., Liu, P., Wang, Y., and Chen, M.W. (2015). Hierarchical nanoporous metal/metal-oxide composite by dealloying metallic glass for high-performance energy storage. Corros. Sci. *96*, 196–202. https://doi.org/10.1016/j.corsci.2015.04.003.

Shi, P., Li, R., Li, Y., Wen, Y., Zhong, Y., Ren, W., Shen, Z., Zheng, T., Peng, J., Liang, X., et al. (2021a). Hierarchical crack buffering triples ductility in eutectic herringbone high-entropy alloys. Science *373*, 912–918. https://doi.org/10.1126/science.abf6986.

Shi, S., Li, Y., Ngo-Dinh, B.-N., Markmann, J., and Weissmüller, J. (2021b). Scaling behavior of stiffness and strength of hierarchical network nanomaterials. Science *371*, 1026–1033. https://doi.org/10.1126/science.abd9391.

Shi, S., Markmann, J., and Weissmüller, J. (2017). Actuation by hydrogen electrosorption in hierarchical nanoporous palladium. Phil. Mag. *97*, 1571–1587. https://doi.org/10.1080/14786435.2017.1311428.

Shi, Y., Zhang, Y., Qin, J., and Zhang, Z. (2020). Macro-/micro-coupling regulation of nanoporous metals via vapor phase alloying-dealloying. Sci. China Mater. *64*, 1521–1533. https://doi.org/10.1007/s40843-020-1546-1.

Sieradzki, K., Dimitrov, N., Movrin, D., McCall, C., Vasiljevic, N., and Erlebacher, J. (2002). The dealloying critical potential. J. Electrochem. Soc. *149*, B370–B377. https://doi.org/10.1149/1.1492288.

Song, T., Yan, M., and Qian, M. (2018). The enabling role of dealloying in the creation of specific hierarchical porous metal structures-A review. Corros. Sci. *134*, 78–98. https://doi.org/10.1016/j.corsci.2018.02.013.

Sun, M.H., Huang, S.Z., Chen, L.H., Li, Y., Yang, X.Y., Yuan, Z.Y., and Su, B.L. (2016). Applications of hierarchically structured porous materials from energy storage and conversion, catalysis, photocatalysis, adsorption, separation, and sensing to biomedicine. Chem. Soc. Rev. *45*, 3479–3563. https://doi.org/10.1039/c6cs00135a.

Wada, T., Geslin, P.-A., and Kato, H. (2018). Preparation of hierarchical porous metals by two-step liquid metal dealloying. Scr. Mater. *142*, 101–105. https://doi.org/10.1016/j.scriptamat.2017.08.038.

Wang, J., You, L., Li, Z., Liu, X., Li, R., Du, Q., Wang, X., Wang, H., Wu, Y., Jiang, S., and Lu, Z. (2021). Self-supporting nanoporous Ni/metallic glass composites with hierarchically porous structure for efficient hydrogen evolution reaction. J. Mater. Sci. Technol. *73*, 145–150. https://doi.org/10.1016/j.jmst.2020.09.016.

Wang, Z., Liu, Y., Tao, P., Shen, Q., Yi, N., Zhang, F., Liu, Q., Song, C., Zhang, D., Shang, W., and Deng, T. (2014). Bio-inspired evaporation through plasmonic film of nanoparticles at the air-water interface. Small *10*, 3234–3239. https://doi.org/10.1002/smll.201401071.

Xing, X.-F., Han, D.-Q., Wu, Y.-F., Guan, Y., Bao, N., and Xu, X.-H. (2012). Fabrication and electrochemical property of hierarchically porous Au-Cu films. Mater. Lett. *71*, 108–110. https://doi.org/10.1016/j.matlet.2011.12.056.

Xue, P., Liu, S., Shi, X., Sun, C., Lai, C., Zhou, Y., Sui, D., Chen, Y., and Liang, J. (2018). A hierarchical silver-nanowire-graphene host enabling ultrahigh rates and superior long-term cycling of lithium-metal composite anodes. Adv. Mater. *30*, 1804165. https://doi.org/10.1002/adma.201804165.

Yang, X.Y., Chen, L.H., Li, Y., Rooke, J.C., Sanchez, C., and Su, B.L. (2017). Hierarchically porous materials: synthesis strategies and structure design. Chem. Soc. Rev. *46*, 481–558. https://doi.org/10.1039/c6cs00829a.

Yilmaz, E.D., Schneider, G.A., and Swain, M.V. (2015). Influence of structural hierarchy on the fracture behaviour of tooth enamel. Philos. Trans. A Math. Phys. Eng. Sci. *373*, 20140130. https://doi.org/10.1098/rsta.2014.0130.

Zhang, J., and Li, C.M. (2012). Nanoporous metals: fabrication strategies and advanced electrochemical applications in catalysis, sensing and energy systems. Chem. Soc. Rev. *41*, 7016–7031. https://doi.org/10.1039/c2cs35210a.

Zhang, L., Lang, X., Hirata, A., and Chen, M. (2011). Wrinkled nanoporous gold films with ultrahigh surface-enhanced Raman scattering enhancement. ACS Nano *5*, 4407–4413. https://doi.org/10.1021/nn201443p.

Zhang, X., Zheng, Y., Liu, X., Lu, W., Dai, J., Lei, D.Y., and MacFarlane, D.R. (2015). Hierarchical porous plasmonic metamaterials for reproducible ultrasensitive surface-enhanced Raman spectroscopy. Adv. Mater. *27*, 1090–1096. https://doi.org/10.1002/adma.201404107.

Zhang, Y., Sun, X., Nomura, N., and Fujita, T. (2019). Hierarchical nanoporous copper architectures via 3D printing technique for highly efficient catalysts. Small *15*, 1805432. https://doi.org/10.1002/smll.201805432.

Zhang, Y., Wang, Y., Yu, B., Yin, K., and Zhang, Z. (2022). Hierarchically structured black gold film with ultrahigh porosity for solar steam generation. Adv. Mater. *34*, 2200108. https://doi.org/10.1002/adma.202200108.

Zhu, L., Gao, M., Peh, C.K.N., and Ho, G.W. (2019). Recent progress in solar-driven interfacial water evaporation: advanced designs and applications. Nano Energy *57*, 507–518. https://doi.org/10.1016/j.nanoen.2018.12.046.

STAR★METHODS

KEY RESOURCES TABLE

REAGENT or RESOURCE	SOURCE	IDENTIFIER
Chemicals, peptides, and recombinant proteins		
Au	Zhongnuo Advanced Material (Beijing) Technology Co., Ltd.	CAS: 7440-57-5
Ag	Zhongnuo Advanced Material (Beijing) Technology Co., Ltd	CAS: 7740-22-4
Zn	Zhongnuo Advanced Material (Beijing) Technology Co., Ltd	CAS: 7440-66-6
Perchlorate acid	Sinopharm Chemical Reagent Co. Ltd	10015161 CAS: 7601-90-3

RESOURCE AVAILABILITY

Lead contact

Further information and requests for resources and reagents should be directed to and will be fulfilled by the lead contact, Zhonghua Zhang (zh_zhang@sdu.edu.cn).

Materials availability

This study did not generate new unique reagents.

Data and code availability

- All data reported in this paper will be shared by the lead contact upon reasonable request.
- This paper does not report original codes.
- Any additional information required to reanalyze the data reported in this paper is available from the lead contact upon request.

EXPERIMENTAL MODEL AND SUBJECT DETAILS

This work did not need any unique experimental model.

METHOD DETAILS

Sample preparation

The $Ag_{95}Au_5$ alloy was prepared by induction melting from Ag (purity: 99.99 wt %) and Au (purity: 99.99 wt %) under vacuum and homogenized at 850°C for 48 h. Then the alloy ingot was further cold-rolled repeatedly until reaching a thickness of 100 μm and annealed at 500°C in vacuum for 5 h to remove the residual stress. To fabricate the Ag-Au-Zn alloy, the Zn powder (99.9 wt.%) of 1 g was first put into the bottom of a quartz tube, then the $Ag_{95}Au_5$ alloy foil was cut into the disk with a diameter of 16 mm and fixed at the middle of the quartz tube to avoid direct touching with Zn powder. After that, the quartz tube was purged by Ar and pumped to vacuum repeatedly for at least 5 times to eliminate the influence of oxygen. Eventually, the quartz tube was sealed by hydrogen flame and heated in a resistance furnace at 550°C for different times to conduct VPA.

The unimodal MP-$Ag_{95}Au_5$ was prepared by VPD of Ag-Au-Zn alloy in a high-temperature tube furnace at 650°C for 1 h after being washed by Ar for at least 5 times. Noticeably, in order to avoid oxidation, the high-temperature tube furnace was also checked the air tightness and the surface of precursor alloy was polished to remove the oxide layer in advance. The pressure of VPA and VPD was 50 Pa. Then the MP-$Ag_{95}Au_5$ was electrochemically dealloyed in a standard three-electrode cell filled with 1 mol L^{-1} $HClO_4$ as the electrolyte on a CHI660E potentiostat at room temperature to fabricate the bimodal nanoporous AgAu alloy (NP-AgAu). The Ag/AgCl electrode, graphite rod and MP-$Ag_{95}Au_5$ served as the reference electrode, counter electrode and working electrode, respectively. The dealloying was performed at a constant potential of 0.65 V (vs. Ag/AgCl) until the current dropped to 50 μA. To fabricate the 3rd hierarchy level porosity and obtain the N^3PG, the bimodal NP-AgAu alloy was first annealed at 500°C for 2 h in vacuum to coarsen the ligaments and pores to the submicron scale, then the as-fabricated sample was

electrochemically dealloyed at 1 V (vs. Ag/AgCl) in 1 mol L^{-1} $HClO_4$ to remove most of Ag. The N^1PG and N^2PG were obtained by directly ECD of the pristine $Ag_{95}Au_5$ alloy foil and MP-$Ag_{95}Au_5$ at 1 V (vs. Ag/AgCl) in 1 mol L^{-1} $HClO_4$.

Microstructural characterization

XRD patterns of all samples were recorded on an XD-3 diffractometer (Beijing Purkinje General Instrument Co., Ltd, China) with Cu Kα radiation. SEM (ZEISS SIGMA 300) equipped with an EDX analyzer and TEM (FEI Titan 80-300) were performed to probe the microstructures and chemical compositions of intermediate and final samples with different hierarchy levels. In addition, the ligament sizes of samples were evaluated using the Nanomeasure software by manually measuring at least 200 ligaments in the SEM and TEM images.

Electrochemical measurements and SSG tests

Electrochemical measurements were carried out in a traditional three-electrode system at room temperature in 1 mol L^{-1} $HClO_4$. To assess the C_{dl}, CVs were recorded in the non-Faradaic region (0.3–0.4 V (vs. Ag/AgCl)) at different scan rates. The C_{dl} was calculated by the following equation:

$$C_{dl} = \Delta_j / v$$

where Δ_j ($\Delta_j = (j_a - j_c)/2$) and v represented the current density (mA cm^{-2}) at 0.35 V (vs. Ag/AgCl) and scan rate (mV s^{-1}), respectively. The charge transfer kinetics of NPG with different hierarchy levels were measured by multi-potential steps. The transients of current, I, versus time, t, followed potential steps from starting electrode potential E_0 = 0 V (vs. Ag/AgCl) for 10 s to final potentials (E_f = 0.1, 0.3, 0.5, 0.8, 1.0 V (vs. Ag/AgCl)) for 30 s.

For the SSG tests, the as-fabricated NPG foils were adhered to the microporous substrate as the plasmonic absorber. The polystyrene foam and cotton were used as the thermal insulator and one-dimensional pathway for water transportation respectively, which could diminish the thermal loss and ensure a continuous water supply. The SSG tests were measured using the xenon lamp (PLS-SXE300+, Beijing Perfectlight Technology Co., Ltd., China) with an AM 1.5G filter and a uniform light modulator (PLSLA320A, Beijing Perfectlight Technology Co., Ltd., China) as a solar simulator. The illumination intensity was calibrated to 1 kW m^{-2} by an optical power meter (PL-MW2000). The real-time mass change of water during the evaporation process was evaluated by an electronic balance (BSA124S-CW, Sartorius, Germany) connected to a computer. The evaporation rate was calculated after 60 min of testing.

QUANTIFICATION AND STATISTICAL ANALYSIS

The ligament size is measured by the Nanomeasure software. And the figures shown in the main text are produced by Origin from the raw data.

ADDITIONAL RESOURCES

Our study has not generated or contributed to a new website/forum or not been a part of a clinical trial.